X-ray-imaging spectrometer (XRIS) for studies of residual kinetic energy and low-mode asymmetries in inertial confinement fusion implosions at OMEGA (invited)

P. J. Adrian ✉; B. Bachmann; R. Betti; ... et. al

Check for updates

CrossMark

View Online

Export Citation

Articles You May Be Interested In

The phase-2 particle x-ray temporal diagnostic for simultaneous measurement of multiple x-ray and nuclear emission histories from OMEGA implosions (invited)

Rev Sci Instrum (October 2022)

Porosity measurement and petrophysical properties of the Indonesian limestone as reservoir rock by using X-ray and neutron imaging technique

AIP Conference Proceedings (November 2021)

An x-ray penumbral imager for measurements of electron–temperature profiles in inertial confinement fusion implosions at OMEGA

Rev Sci Instrum (April 2021)

Review of Scientific Instruments

AIP Publishing

X-ray-imaging spectrometer (XRIS) for studies of residual kinetic energy and low-mode asymmetries in inertial confinement fusion implosions at OMEGA (invited)

View Online   Export Citation   CrossMark

P. J. Adrian,[1,a] [ID]   B. Bachmann,[2] [ID]   R. Betti,[3]   A. Birkel,[1] [ID]   P. V. Heuer,[3] [ID]   M. Gatu Johnson,[1] [ID]
N. V. Kabadi,[1]   J. P. Knauer,[3]   J. Kunimune,[1] [ID]   C. K. Li,[1]   O. M. Mannion,[4] [ID]   R. D. Petrasso,[1] [ID]   S. P. Regan,[3] [ID]
H. G. Rinderknecht,[3] [ID]   C. Stoeckl,[1] [ID]   F.H. Séguin,[1]   A. Sorce,[3]   R. C. Shah,[3]   G. D. Sutcliffe,[1] [ID]   and J. A. Frenje[1] [ID]

AFFILIATIONS

[1] Plasma Science and Fusion Center, MIT, Cambridge, Massachusetts 02139, USA
[2] Lawrence Livermore National Laboratory, Livermore, California 94550, USA
[3] Laboratory for Laser Energetics, University of Rochester, Rochester, New York 14623, USA
[4] Sandia National Laboratories, Albuquerque, New Mexico 87185, USA

Note: This paper is part of the Special Topic on Proceedings of the 24th Topical Conference on High-Temperature Plasma Diagnostics.
[a]Author to whom correspondence should be addressed: pjadrian@mit.edu

ABSTRACT

A system of x-ray imaging spectrometer (XRIS) has been implemented at the OMEGA Laser Facility and is capable of spatially and spectrally resolving x-ray self-emission from 5 to 40 keV. The system consists of three independent imagers with nearly orthogonal lines of sight for 3D reconstructions of the x-ray emission region. The distinct advantage of the XRIS system is its large dynamic range, which is enabled by the use of tantalum apertures with radii ranging from 50 μm to 1 mm, magnifications of 4 to 35×, and image plates with any filtration level. In addition, XRIS is capable of recording 1–100's images along a single line of sight, facilitating advanced statistical inference on the detailed structure of the x-ray emitting regions. Properties such as P0 and P2 of an implosion are measured to 1% and 10% precision, respectively. Furthermore, T_e can be determined with 5% accuracy.

I. INTRODUCTION

Inertial Confinement Fusion (ICF) implosion designs accelerate a deuterium–tritium (DT) ice shell inward via laser ablation to compress a low-density DT gas at the center to ignition conditions.[1] The low-density gas forms a hotspot, which propagates a burn wave into the surrounding high-density fuel. These implosions routinely create burning plasmas at the National Ignition Facility (NIF), when alpha particle heating is exceeding the heating due to mechanical work by the imploding shell.[2,3] Controlling degradation mechanisms such as low-mode asymmetry of the shell and mixing

of hotspot and shell are critical to implosion performance.[4] Low-mode asymmetry of the shell causes the inefficient conversion of shell kinetic energy to hot-spot kinetic energy, which greatly limits performance. Mixing between the hotspot and shell is caused by shell instabilities, target defects, and engineering features that limit performance through increased radiation losses.[5–7]

X-ray imaging spectroscopy is a critical diagnostic technique to diagnose implosion performance through measurements of hot-spot temperature, shape, and mix level;[5,8–10] for example, x-ray spectral measurements are used to measure the thermal electron temperature of the hotspot, T_e.[5,8,10] Previous studies have diagnosed residual

kinetic energy in the hotspot by comparing T_e measurements to ion temperature measurements, T_{DT}, made with neutron time-of-flight (nTOF) detectors.[10] In addition, x-ray imaging diagnoses the overall shape of the hotspot, which is used to empirically control the drive asymmetry on different ICF platforms. Furthermore, localized bright regions are routinely seen in x-ray self-emission images.[11] The bright regions are generated from the injection of outside material into the hotspot. X-ray imaging spectroscopy provides spatially resolved T_e measurements that have shown these localized bright emission regions to be cooler than the surrounding hotspot.[5]

X-ray penumbral imaging is the standard imaging technique used in x-ray imaging spectroscopy. Penumbral imaging is a coded imagining technique where the size of the aperture, D, is larger than the emitting source size, r_S ($D > r_S$). The recorded penumbral image, P, consists of an umbra and penumbra. The umbra region of differentially filtered images is typically used to measure the total emitted x-ray brightness and a spatially averaged, T_e.[8] The penumbral region contains all the information about the source distribution. Penumbral imaging is attractive because it can work at lower photon yields and possesses higher signal-to-noise as compared to pinhole imaging under certain conditions.[9] In addition, the penumbral image contains redundancy and thus is resistant to single pixel corruption, unlike pinhole imaging.

This work describes the implementation and use of the x-ray Imaging Spectrometer (XRIS) on OMEGA,[12] and the resulting data obtained. XRIS can be operated in multiple configurations specialized to the experiment. This work describes upgrades to the

hardware, which enable 35× magnification. This high magnification mode of XRIS enables imaging with spatial resolutions down to the diffraction limit of the aperture. Furthermore, XRIS can be operated with three nearly orthogonal lines of sight, enabling the 3D structure of the hotspot to be probed. In addition, XRIS is a perfect complement to the phase-2 Particle x-ray Temporal Diagnostic (PXTD-2),[13] which is used to measure time resolved x-ray emission histories in different energy bands. The x-ray emission imaged with XRIS combined with the time resolved PXTD provides a dynamic picture of x-ray emission from the hotspot.

The structure of this paper is as follows: Sec. II describes the XRIS hardware and implementation. Section III describes different 2D reconstruction routines and contrasts their performance. Section IV discusses the different measurements possible with the different XRIS configurations. Section V concludes and details future plans with XRIS.

II. XRIS HARDWARE

XRIS is fielded in a Ten-inch Manipulator (TIM), which holds the penumbral aperture at various stand-off distances from the implosion and houses the image plate detectors. Figure 1(a) displays the full XRIS diagnostic as it is housed in the TIM enclosure. The image-plate detector can be fielded in two locations, one for low magnification and one for high magnification.

The low-magnification configuration positions the detector at a fixed distance of 0.59 m away from the location of the aperture. This configuration is used for a charged particle imaging system
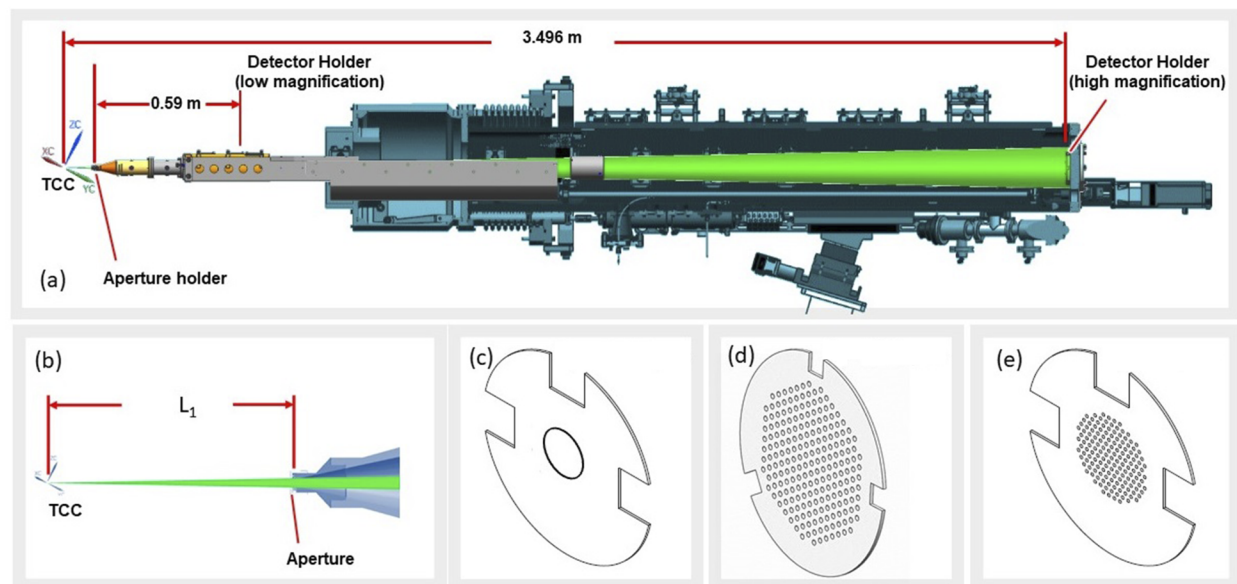
FIG. 1. Schematic of XRIS hardware. (a) Full schematic of XRIS in an OMEGA Ten-inch Manipulator (TIM) insertion module. The farthest detector holder (high magnification) is positioned at the back end of the TIM at 3.496 m from Target Chamber Center (TCC). The second in-close detector holder (low magnification) is positioned at a distance of 0.59 m from the aperture. (b) Zoom-in of the aperture holder, which positions an aperture at a variable distance, L_1, from TCC. (c) A single $R_a = 1000$ μm aperture. (d) An array of 212 apertures with $R_a = 150$ μm. (e) An array of 151 apertures with $R_a = 50$ μm.

discussed in Refs. 14–16. Generally, an aperture can be fielded up to 4 cm away from the implosions, enabling magnifications up to $M = 59/4 = 14.75\times$. The detection area for this configuration is a 7 cm diameter region.

New to this work is the ability to use a high magnification detector positioned at the back end of the TIM at a distance of 3.496 m from TCC. The detector area is 10×10 cm^2. The high magnification detector is primarily used for x-ray imaging of cryogenic layered DT implosions. The cryostat hardware that cools the capsule limits the minimum target to aperture distance to about 10 cm at OMEGA. Thus, the high magnification detector images at a magnification of $M \approx 35\times$ for cryogenic targets. At this magnification, the spatial resolution of the detector is primarily dictated by blurring due to x-ray diffraction.[9]

XRIS is routinely run along multiple lines-of-sight for diagnosing implosions at OMEGA. Figure 2 shows the orientation of the three lines of sight of XRIS in the OMEGA target chamber. XRIS 1, 2, and 3 were run in TIMs 2, 4, and 5, respectively. The angle between each pair of TIMS is about 90°. Obtaining orthographic projections is critical for 3D reconstructions of the x-ray emission.

Three types of apertures are commonly used in XRIS. The first aperture is a single 1000 μm radius aperture shown in Fig. 1(c). This large aperture guarantees that $D > r_S$ for most typical implosions at OMEGA. The second aperture consists of an array of 212 apertures with a 150 μm radius [Fig. 1(d)]. The third aperture consists of an array of 151 apertures with radii of 50 μm [Fig. 1(e)]. This design was intended for small source sizes with faint signals. The use of an aperture array allows for many images to be collectively analyzed to substantially improve signal to noise.

XRIS runs with Fuji ^{TM} image plates as the detector.[17] The kinematic bases for both the low and high magnification detectors allow for multiple image plates and filters to be fielded. The filtration for each image plate is chosen by the user to capture energy bands of interest. Figure 1 of Ref. 8 displays the detector response. XRIS is also capable of running with other solid state detectors, such as CR39. The CR39 is used to detect charged particles generated from an implosion that passes through the apertures.
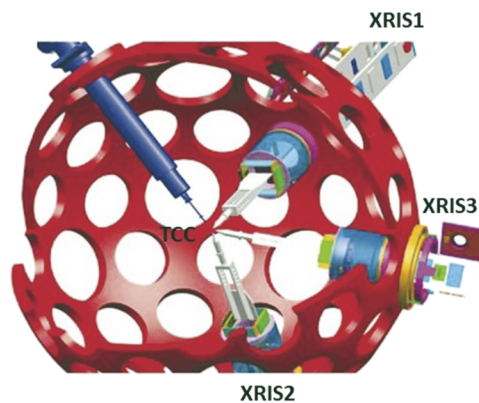

FIG. 2. Drawing of three XRIS systems in nearly orthogonal lines of sight on OMEGA.

III. RECONSTRUCTION TECHNIQUES AND PERFORMANCE

Penumbral imaging of x rays is equivalent to parallel beam projection tomography if the distance between source and aperture is much greater than the size of the source (paraxial approximation), and the attenuation of the x-ray is negligible in the source.[18] With this set of constraints, the penumbral image, P, recorded by a detector is a convolution of the brightness profile, B, and the aperture point spread function, A,

$$P(X, Y) = B(X, Y) \times A(X, Y), \tag{1}$$

where X and Y are the Cartesian coordinates in the detector plane. The coordinates in the source plane are $x = X/M$ and $y = Y/M$. For a sharp-edge aperture of radius R_{app}, the point spread function is

$$A(X, Y) = \begin{cases} 1, & X^2 + Y^2 \leq R_0^2, \\ 0 & \text{otherwise,} \end{cases} \tag{2}$$

where $R_0 = R_{app}(M + 1)$. The surface brightness, B, is a line integral through the emissivity function, S, such that

$$B(x, y) = \int_{-\infty}^{\infty} S(x, y, z) dz, \tag{3}$$

where the z direction is taken to be the imaging direction.

A method to deconvolve A from P is required to obtain B. A direct way is to compute B from Fourier transforms of P and A,

$$B = \mathcal{F}^{-1}\left[\frac{\mathcal{F}[P]}{\mathcal{F}[A]}\right], \tag{4}$$

where $\mathcal{F}$ and $\mathcal{F}^{-1}$ are the Fourier and inverse Fourier transforms. However, Eq. (4) can rarely be used with real data because it is extremely sensitive to noise and finite counting statistics. In practice, image reconstruction is performed with special algorithms for the deconvolution problem.

A. Wiener deconvolution

Wiener deconvolution is a popular method to use as it can deal with the noise problems inherent to Fourier-transform methods of deconvolution.[19] A strength of the Wiener deconvolution method is that information about the spectral-noise content is included in the deconvolution. For white noise, the Wiener deconvolution is

$$B = \mathcal{F}^{-1}\left[\frac{\mathcal{F}[P]}{\mathcal{F}[A]} \frac{\mathcal{F}[A]^2}{\mathcal{F}[A]^2 + NSR}\right], \tag{5}$$

where NSR is the total noise to signal power ratio. Generally, NSR is not *a priori* known in penumbral imaging and is difficult to quantify from raw data. X-ray penumbral imaging with imaging plates poses multiple sources of noise due to finite photon statistics, neutron hits, and micro scratches in the phosphor layer of the image plate.

Therefore, the NSR, in practice, is a fitting parameter, which controls the attenuation of high spatial frequency content in a reconstructed image.

B. Convolution and backprojection

The XRIS images tomographic cords across the image plane, enabling the use of convolution and back-projection methods of computed tomography (CT). These backprojection methods have been used in both x-ray and charged particle penumbral imaging.[9,14–16] The back-projection method leverages the Fourier convolution theorem and Fourier-slice theorem to relate B to the radial derivative of P as

$$B = \mathcal{R}^{-1}\left[\frac{dP(X - R_0, Y - R_0)}{dR}\right], \tag{6}$$

where $\mathcal{R}^{-1}$ is the inverse-Radon transform and $R = \sqrt{X^2 + Y^2}$. However, the back-projection method is only applicable if $R_{app} \ll r_S$. Seguin et al.[14] developed a back projection method, which corrects for the circularity of the aperture when $R_{app} \sim r_S$. In Seguin's method, B is computed as

$$B \approx \int_0^{2\pi} w P'\left(R' - M(x \cos\phi + y \sin\phi), \phi\right) d\phi, \tag{7}$$

where

$$w = 1 - M(x, \cos\phi + y \sin\phi), \tag{8}$$

$$R' = \sqrt{R_0^2 - M^2(x \cos\phi + y \sin\phi)^2}, \tag{9}$$

$$P'(R, \phi) = -\frac{1}{2\pi} C(r) \frac{dP^\star(R, \phi)}{dR}, \tag{10}$$

$$P^\star = P \times F_{smooth} \times F_{CT}. \tag{11}$$

The function $C(r)$ is defined by Eq. (7) in Ref. 14. In this algorithm, the penumbral image, P, is both smoothed and filtered through convolution with $F_{smooth} = \exp(-(r/\sqrt{2}r_{smooth})^2)$ and F_{CT}, where $F_{CT}(r)$ is the ramp filter defined by $\mathcal{F}(F_{CT}) = |k|$. Here, r_{smooth} is a free parameter that sets the spatial resolution of the reconstruction.

C. Richardson–Lucy deconvolution

Another popular deconvolution method is the Richardson–Lucy (RL) method.[20,21] This method is a gradient-descent method, which finds the maximum-likelihood solution of Eq. (1). The RL method is widely used in astronomy because it can handle Poisson statistics when imaging weak signals.[22,23] Furthermore, it forces the surface brightness to be non-negative and preserves the total number of counts comprising the image. The RL algorithm is iterative where the "$k + 1$" iteration is

$$B_{k+1} = B_k\left[A\frac{P}{A \times B_k}\right]. \tag{12}$$

The iteration can be started by starting with an initial guess of B_1 for the image, which can be a flat field brightness profile. The RL method is slow, requiring many iterations to minimize the mean-squared-error of the model compared to measurement. Therefore, acceleration methods have been pursued to speed up the RL method. This work uses the acceleration method proposed by Biggs and Andrews.[24]

D. Reconstruction algorithm performance

All reconstruction methods presented above amplify noise in the reconstructed image and have free parameters, which impact the quality of the reconstructed surface brightness. It is critical to understand the spatial resolution and noise amplification properties of each reconstruction algorithm. The back-projection method is unique because its free parameter, r_{smooth}, sets the amount of spatial blurring in the final reconstruction. However, there is no obvious significance to the number of iterations of the RL deconvolution nor the NSR of the Wiener deconvolution. Furthermore, interpreting a reconstructed surface brightness requires understanding the mapping of noise and background from the penumbral image and of the surface brightness. Numerical studies using synthetic penumbral images are used to address these problems below.

Figure 3(a) shows a penumbral image generated from the convolution of a square surface brightness [Fig. 3(b)] and a circular aperture. The image in Fig. 3(a) was generated at a magnification of 35× using a $R_{app} = 150\ \mu m$ aperture. The penumbral image was normalized such that both the penumbral image and the surface brightness had a maximum value of one. The penumbral image was subsequently degraded by adding a uniform background of white noise. The signal to the background level was set to 10 with a standard deviation of 0.01. This level of degradation is typical of observations of XRIS data obtained from cryogenic DT implosions at OMEGA.

The surface brightness was subsequently reconstructed from the penumbral image in Fig. 3(a) using the three deconvolution algorithms presented above. Each row in Fig. 4 displays the results from one of the routines, whereas the columns display the spatial resolution, δx, achieved through different parameter choices for each algorithm. The top row of Fig. 3(a) displays the surface brightness obtained with the Wiener deconvolution algorithm for different choices of NSR. This study demonstrates that the choice of NSR sets δx, where larger values blur the image. In addition, this algorithm
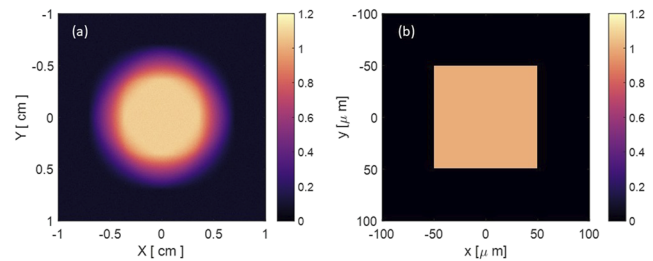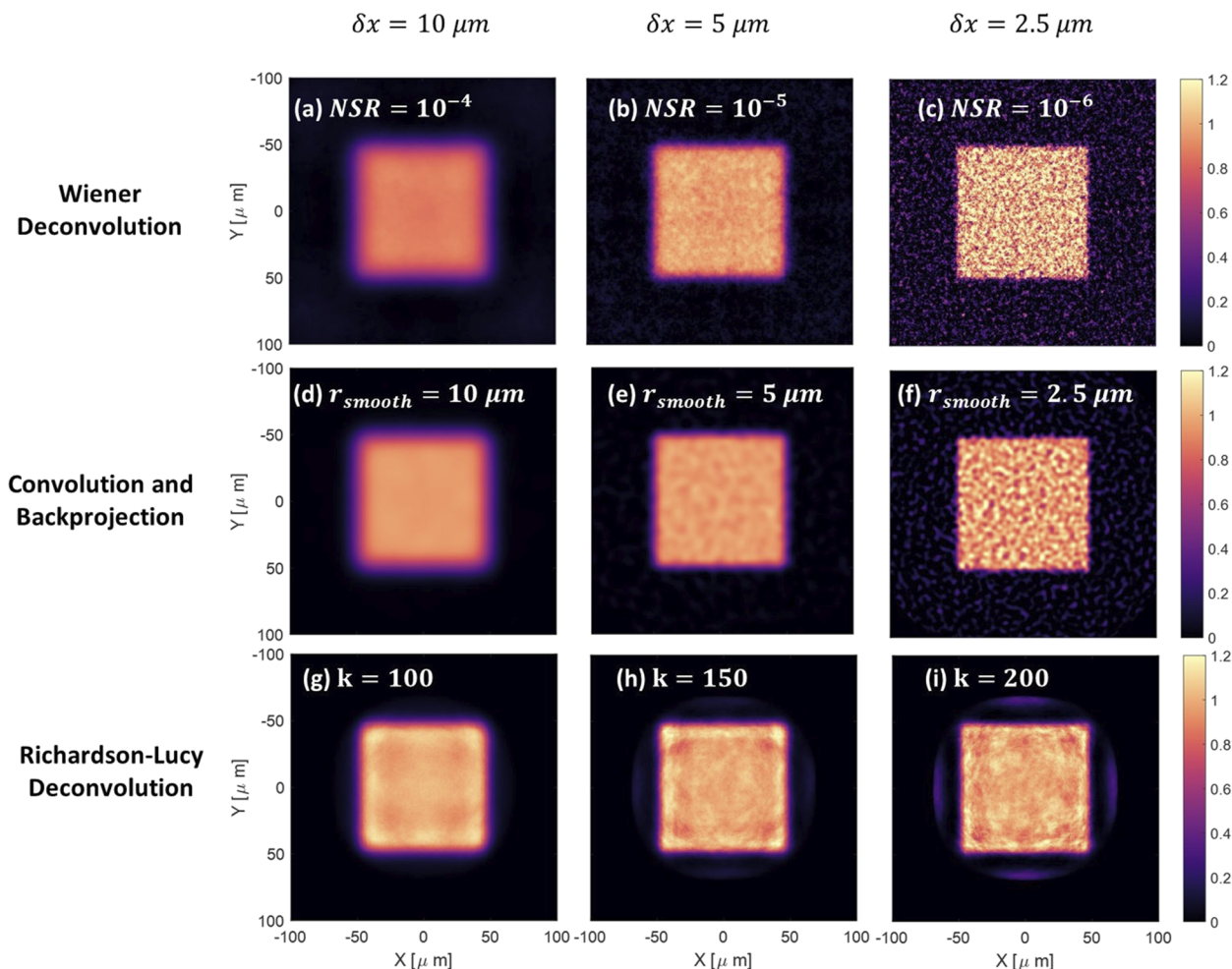

FIG. 3. (a) Penumbral image used in synthetic data study. (b) Brightness profiles used to generate a penumbral image in (a).

FIG. 4. Reconstructed surface brightness images using the three reconstruction algorithms using the penumbral image from Fig. 3(a). Panels (a)–(c) display the Wiener deconvolution results for NSR values of 1×10^{-4}, 1×10^{-5}, and 1×10^{-6}, respectively. Panels (d)–(f) display the convolution and backprojection results for r_{smooth} values of 10, 5, and 2.5 μm, respectively. Panels (g)–(i) display the Richardson–Lucy results for iteration k values of 100, 150, and 200, respectively. The columns represent a reconstruction done to a spatial resolution, $\delta x = 10$, 5, and 2 μm from left to right.

maps the white noise of the penumbra image into high frequency noise. The noise is uniform in amplitude over the surface brightness. Similar behavior is seen in the performance of the convolution and backprojection algorithm results, which are displayed in the middle row of Fig. 4. For this algorithm, the spatial resolution of the resulting surface brightness is simply specified by r_{smooth}. As r_{smooth} decreases, a uniform amplitude noise is also observed to degrade the surface brightness reconstruction. However, comparing Figs. 4(c) and 4(f), it is observed that the spatial structure of the noise is more "lumpy" for the backprojection than the Wiener deconvolution. The "lumpy" nature of the noise is primarily due to the smoothing of the penumbral image in the backprojection method, which excludes high-mode noise from the solution.

A significant deviation in behavior is observed in the results of the RL deconvolution as displayed in the bottom row of Fig. 4. The spatial resolution of the reconstruction decreases as more iterations of the RL algorithm are done. However, the RL algorithm does not map the uniform noise in the penumbral image to uniform noise in the reconstitution, like the Wiener and backprojection algorithms. There is also notably less high frequency noise in the RL reconstruction than in the two other algorithms. This is apparent in Fig. 4(f) where a significant circular aberration is observed at a radius of ~60 μm around the square surface brightness profile. The RL algorithm generates this aberration through its positive definite constraint on the reconstruction. As the RL iterates, pixels in the solution that reach zero emission are then excluded from the surface brightness at the next iteration. This builds up groups of dead pixels that cannot be used in the surface brightness. Pixels in the periphery of the image are subsequently used to try to fit noise, resulting in the observed aberrations.

Overall, the numerical studies presented in this section are critical for identifying data features in reconstructed surface brightness images and excluding aberrations or noise. However, a remaining challenge is the choice of the free parameters in each algorithm when reconstructing data where the surface brightness is not known. There are no known universal termination conditions for any algorithm. Generally, achieving high spatial resolution in the reconstruction comes at the cost of increasing the high-mode noise or introducing spurious aberrations. In this work, data are analyzed with all three algorithms. Numerical studies were done for each configuration of XRIS to determine the spatial resolution set by the three reconstruction algorithms. The reconstruction algorithms were run until they achieved a spatial resolution that was either limited by the pixel size, $\delta x \approx (25\ \mu m)/M$, or x-ray diffraction, $\delta x \approx \sqrt{\lambda L_1}$, where λ is the average x-ray wavelength.

IV. SAMPLE DATA AND ANALYSIS

Example data obtained with different XRIS configurations are shown in this section. All examples used SR-type image plates that were scanned at 25 μm with sensitivity S1000.[25] The fade of each image plate has been corrected based on the shot-to-scan time using fade curves reported in Ref. 26.

A. 3D imaging capability

XRIS was fielded in three nearly orthogonal lines of sight using the TIM 2, 4, and 5 to diagnose a DT implosion at OMEGA (shot 96 219). Figure 5(a) depicts the capsule dimensions as well as the laser pulse. The implosion was an ambient target with an outer radius of 445 μm filled with 20 atm DT gas in a 21 μm deuterated polystyrene (CD) shell. The laser pulse was a 1 ns square pulse.

Figure 2 shows the orientation of the three lines of sight of XRIS. XRIS was fielded with 50 μm aluminum and 1500 μm CR39 filters in front of the image plate. Figures 5(b)–5(d) show the measured penumbral images recorded with the 1000 μm aperture at a magnification of 14.5×. The surface brightness was reconstructed from the measured images using the RL algorithm, which was iterated until the spatial resolution was estimated to be 6 μm. Figures 5(e)–5(g) display the reconstructed surface brightness along the three nearly orthogonal lines of sight. In addition, the 17% contour is shown by a dashed red curve in each image along with the P0 through P6 Legendre mode fit of the 17% contour.

Hot-spot volume is a key implosion parameter to diagnose because it is critical to determine the plasma pressure achieved through compression, which is a key performance metric for ignition.[27] The surface brightness images presented in Fig. 5 demonstrate the necessity of 3D reconstruction when determining the x-ray emitting volume. 3D low-mode asymmetries prevent accurate volume determination using only one line of sight.

Future work will involve full 3D reconstruction using XRIS data. While there exist mature 3D reconstruction codes, they often invoke an axis of symmetry of the implosion.[18] 3D reconstructions at OMEGA will require algorithms that do not set such constraints.

B. Utilizing multiple penumbral images

Figure 6 displays XRIS data from shot 97 587, a cryogenic layered DT implosion with a radius of 466 μm with a 32.7 μm thick ice layer and an 8 μm deuterated polystyrene ablator (CD). Figure 6(a) shows the shaped laser pulse used to implode the capsule. XRIS was run with the $151 \times 50\ \mu m^2$ aperture array using the high magnification detector. The image plate was filtered with 500 μm of Aluminum and 1500 μm of CR39. The recorded penumbral images are shown
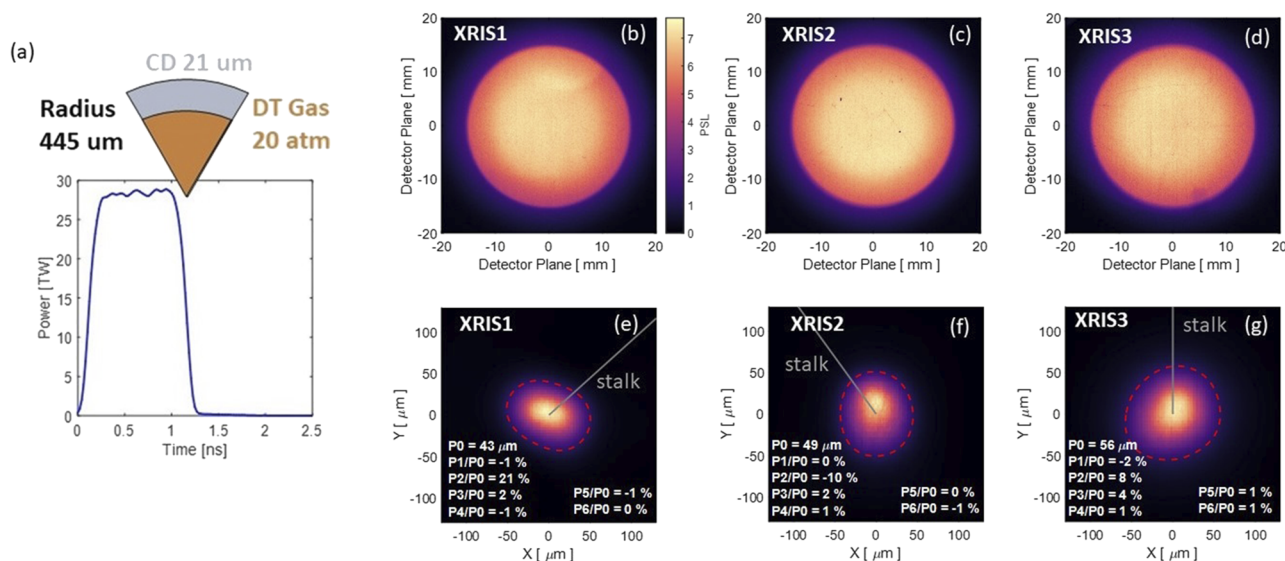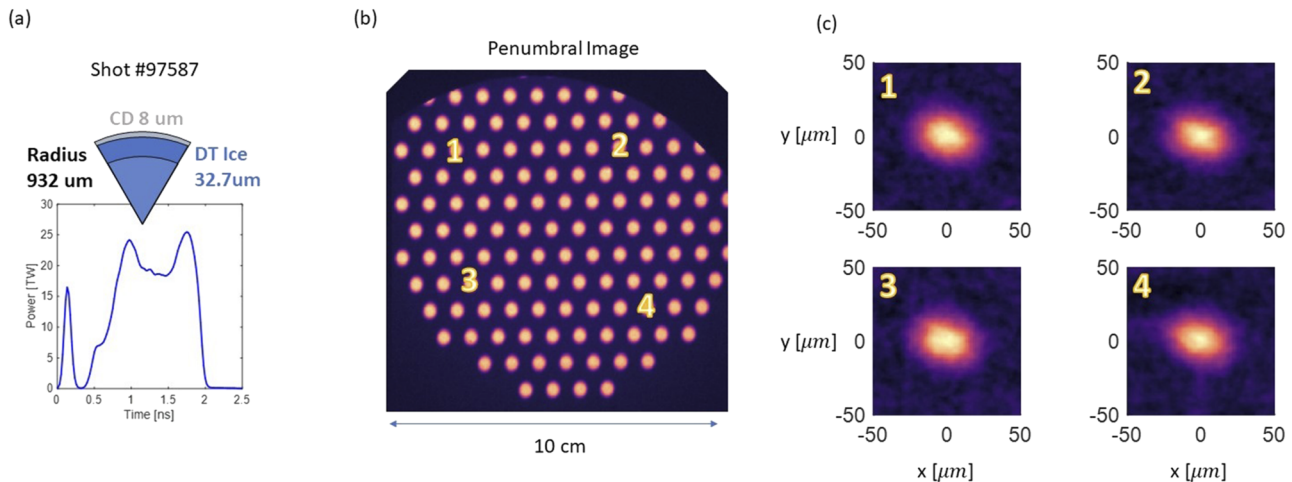
FIG. 5. Sample XRIS data from an ambient DT implosion (shot 96 219). (a) The capsule dimensions, fill, and laser pulse. Panels (b)–(d) show the raw penumbral images measured from three XRIS systems at nearly orthogonal lines of sight using a 1000 μm radius aperture at a magnification of 14.5×. Panels (e)–(g) show the reconstructed surface brightness profile from each line of sight.

FIG. 6. Sample data from shot 97 587. (a) Capsule dimensions and composition as well as the laser pulse. (b) The raw penumbral data recorded by XRIS using an aperture array of 50 μm radius holes. (c) Sample reconstructions from individual penumbral images that have been enumerated in the figure.

in Fig. 6(b). The magnification was 34.0× and was inferred from the distance between penumbral images recorded in the detector plane.

Each penumbral image is reconstructed independently to obtain the surface brightness. Parallax effects from off-axis apertures in the aperture array are negligible. These effects are of order $1 - \cos\beta$, where β is the angle formed between the center penumbral image and the furthest penumbra image. For this detector array, $\beta \approx \arctan(1400/10 \times 10^4 \ \mu m) \approx 0.8°$ parallax distortions are of the order $9 \times 10^{-5} \ll 1$, which is negligible. Figure 6(c) depicts the surface brightness reconstructed from four different penumbral images enumerated 1, 2, 3, and 4 in Figs. 6(b) and 6(c).

All ~113 penumbral images in Fig. 6(b) were reconstructed to understand statistical variations in the reconstruction of the surface brightness. The source size, P0, and mode-2 asymmetry, P2, are determined by fitting associated Legendre polynomials to the 17% contour of all images. Figures 7(a) and 7(b) display histograms of the measured P0 and P2, respectively. The variations observed in P0 and P2 are due to noise, photon counting statistics, and the variation in penumbral hole size/uniformity. These data demonstrate the P0

and P2 of the hotspot and are determined to 1% and 10% precision, respectively.

### C. T_e analysis in multiple lines of sight

Three XRIS systems were fielded using an array of 212 apertures with 150 μm TIM 2, 3, and 5 radii at magnifications of 20×, 25×, and 35×, respectively. Each XRIS was set up with a detector pack in the high-magnification position consisting of 10 μm Tantalum, 1500 μm CR39, an SR image plate, 250 μm Aluminum, and another SR image plate. The emitted x-ray energy spectra are inferred from the measured x-ray energy deposited on the two differentially filtered penumbral images. Reference 8 details the reconstruction of the x-ray energy spectra including the error analysis. The x-ray spectrum was modeled by using a thermal Bremsstrahlung emission profile, which scales as $\propto \exp(-\hbar\nu/T_e)$, where $\hbar\nu$ is the photon energy. A burn-averaged T_e was inferred using the penumbral images detected on each plate along the different lines of sight. Figure 8 shows the T_e measured in the TIM 2, 3, and 5 lines of sight. As shown in Fig. 8, no line-of sight variations of the electron temperature are observed because the emitted x rays are unaffected by hotspot bulk motions. Opacity does not impact the emitted spectrum because the x rays observed have an average energy of 15 keV and are optically thin.[28] However, large differences are observed between the measured T_e and T_{DT}, inferred from the 12 m neutron time-of-flight (nTOF).[29] It is well documented that nTOF inferences of ion temperature are systematically inflated by residual flows that Doppler broaden the DT-neutron energy spectrum.[10,30] The difference between T_e and T_{DT} is currently being studied to assess the levels of residual kinetic energy.[28]

D. Simultaneous XRIS and emission-history measurements of implosions at OMEGA

The XRIS system was used simultaneously with the particle/x-ray temporal diagnostic (PXTD), which is capable of measuring
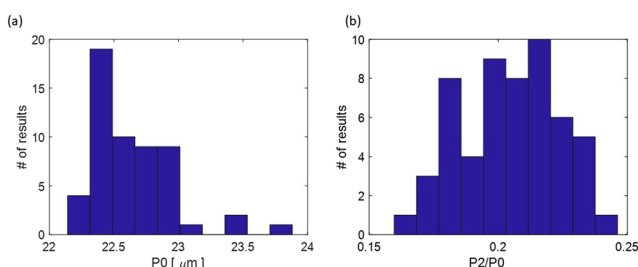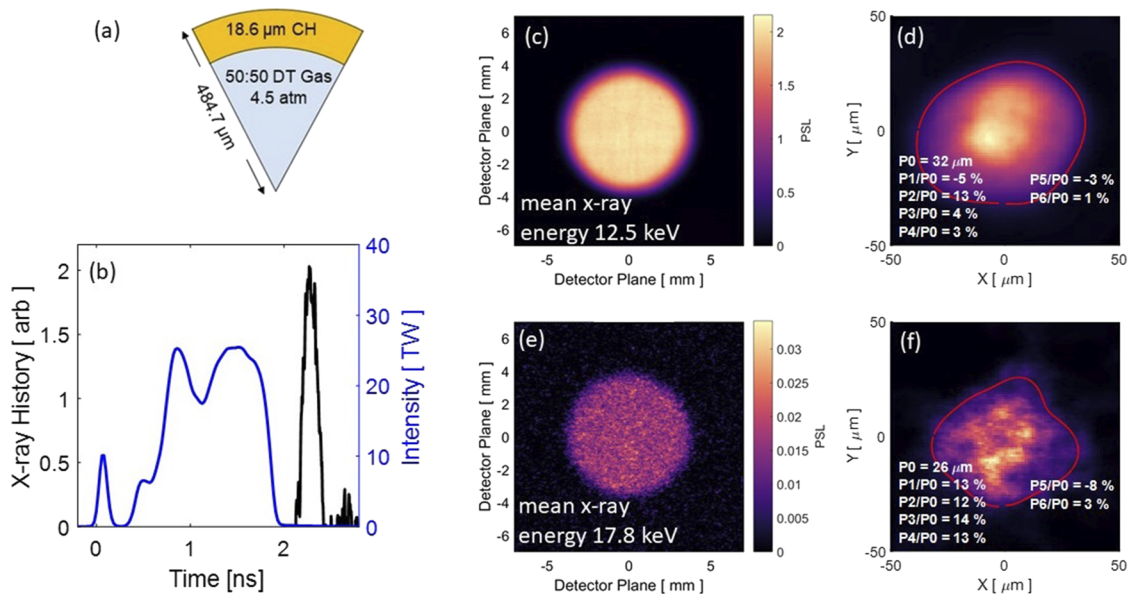

FIG. 7. Inference of P0 = 22.6 ± 0.3 μm (a) and P2 = 20 ± 2% (b) from the 113 images recorded from shot 97 587. The P0 and P2 were determined from the 17% contour of the reconstructed x-ray surface brightness.
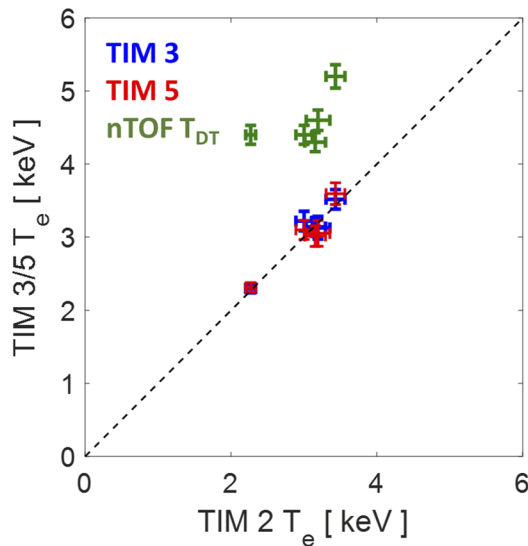
FIG. 8. Burn-averaged T_e measured with XRIS along the TIM 2, 3, and 5 lines of sight for a set of five cryogenic DT implosions 102 559–102 571. For comparison, the DT ion temperature values (green) measured with the 12 m nTOF system at OMEGA are also shown.

x-ray emission histories in multiple energy bands[13,31] to diagnose a series of implosions. Details about the upgraded PXTD are found in Ref. 31. The combination of x-ray images and emission histories is a powerful set of data for constraining simulations and models.

Figure 9 displays data taken by XRIS and PXTD for shot 100 521 at OMEGA. In this experiment, a 484.7 μm radius capsule with an 18.6 μm CH ablator filled with 4.5 atm DT gas was imploded with the laser intensity profile given in Fig. 9(b). The PXTD measured the x-ray emission history of photons with a median energy of ~10 keV [black curve in Fig. 9(b)]. Simultaneously, XRIS was run using an array of 212 apertures with a 150 μm radius. The magnification of XRIS was 25.0×. Two XRIS images are shown in Figs. 9(c) and 9(e), which were generated by photons with a median energy of 12.5 and 17.8 keV and a Full-Width-Half-Max of 5 and 3 keV, respectively. Figures 9(d) and 9(f) display the surface brightness profile reconstructed from the measured images using the RL algorithm to 4 μm resolution.

The data collected by XRIS and PXTD provide a wealth of information, including the x-ray burn width, bang-time, burn volume, and electron temperature, which can be used to test implosion models. Bayesian inference techniques have been used to compare models to data obtained with multiple diagnostics.[32] Recently, Ruby et al.[33] demonstrated a technique that utilized simultaneous measurements of spatially and temporally resolved x-ray self emission from the hotspot to constrain electron heat conduction transport models. Future work will utilize the Bayesian inference technique proposed in Ref. 33 to study electron heat conduction with data simultaneously recorded with XRIS and PXTD.

V. CONCLUSIONS AND OUTLOOK

In summary, XRIS is a multi-functional penumbral imaging system that is used to spatially resolve x-ray emissions in different energy bands through differential filtering. Each system can be fielded in any TIM on OMEGA for imaging along multiple lines of

FIG. 9. XRIS and PXTD sample data from shot 100521. (a) Capsule diagram. (b) Time history of the laser pulse (blue) and measured x-ray emission history (black). (c) and (e) X-ray penumbral images recorded by XRIS with mean x-ray energies of 12.5 and 17.8 keV, respectively. (d) and (f) Reconstructions of the surface brightness profile from (c) and (e), respectively, with 4 μm resolution using the Richardson–Lucy algorithm.

sight. A high magnification system enabling x-ray imaging down to 3 μm spatial resolution has been developed for implosions that require the OMEGA cryostat. XRIS records multiple images using an array of apertures along a single line of sight, enabling statistical inference of hot-spot properties. Properties such as P0 and P2 of an implosion are measured to 1% and 10% precision, respectively. XRIS is readily fielded along multiple lines of sight to image the 3D morphology of the hotspot. XRIS compliments a variety of other x-ray diagnostics in use at OMEGA. Furthermore, T_e can be determined with 5% accuracy.

Future work with XRIS will involve creating a robust 3D reconstruction algorithm. This will enable accurate estimation of implosion properties, such as burn volume, which is difficult to diagnose along one line of sight due to 3D-low-mode asymmetries. Further analysis of 3D x-ray emission in different energy bands will help identify mixed mechanisms through the analysis of T_e profiles. In addition, combining XRIS with other x-ray diagnostics, such as PXTD, will be critical to building a holistic picture of the hotspot.

ACKNOWLEDGMENTS

AUTHOR DECLARATIONS

Conflict of Interest

The authors have no conflicts to disclose.

Author Contributions

P. J. Adrian: Conceptualization (lead); Data curation (lead); Formal analysis (lead); Methodology (lead); Writing – original draft (lead); Writing – review & editing (equal). **B. Bachmann**: Conceptualization (equal). **R. Betti**: Project administration (equal). **A. Birkel**: Data curation (equal). **P. V. Heuer**: Formal analysis (supporting). **M. Gatu Johnson**: Funding acquisition (equal). **N. V. Kabadi**: Data curation (equal). **J. P. Knauer**: Data curation (equal). **J. Kunimune**: Formal analysis (equal). **C. K. Li**: Funding acquisition (equal). **O. M. Mannion**: Data curation (equal). **R. D. Petrasso**: Funding acquisition (equal). **S. P. Regan**: Data curation (equal); Funding acquisition (equal). **H. G. Rinderknecht**: Data curation (equal). **C. Stoeckl**: Data curation (equal). **F. H. Séguin**: Formal analysis (equal); Funding acquisition (equal). **A. Sorce**: Data curation (equal). **R. C. Shah**: Data curation (equal); Formal analysis (equal). **G. D. Sutcliffe**: Data curation (equal). **J. A. Frenje**: Conceptualization (equal); Funding acquisition (equal); Project administration (equal); Supervision (equal); Writing – review & editing (equal).

DATA AVAILABILITY

The data that support the findings of this study are available from the corresponding author upon reasonable request.

REFERENCES

[1] J. Lindl, Phys. Plasmas **2**, 3933 (1995).
[2] A. B. Zylstra *et al.*, Nature **601**, 542 (2022).
[3] A. L. Kritcher *et al.*, Nat. Phys. **18**, 251 (2022).
[4] D. T. Casey *et al.*, Phys. Plasmas **28**, 042708 (2021).
[5] B. Bachmann *et al.*, Phys. Rev. E **101**, 033205 (2020).
[6] T. Ma *et al.*, Rev. Sci. Instrum. **83**, 10E115 (2012).
[7] M. Gatu Johnson *et al.*, Phys. Plasmas **27**, 032704 (2020).
[8] P. J. Adrian *et al.*, Rev. Sci. Instrum. **92**, 043548 (2021).
[9] B. Bachmann *et al.*, Rev. Sci. Instrum. **87**, 11E201 (2016).
[10] L. C. Jarrott *et al.*, Rev. Sci. Instrum. **87**, 11E534 (2016).
[11] G. A. Kyrala *et al.*, Rev. Sci. Instrum. **81**, 10E316 (2010).
[12] T. R. Boehly *et al.*, Opt. Commun. **133**, 495 (1997).
[13] H. Sio *et al.*, Rev. Sci. Instrum. **87**, 11D701 (2016).
[14] F. H. Séguin *et al.*, Rev. Sci. Instrum. **75**, 3520 (2004).
[15] F. H. Séguin *et al.*, Phys. Plasmas **23**, 032705 (2016).
[16] F. H. Séguin *et al.*, Phys. Plasmas **13**, 082704 (2006).
[17] M. J. Rosenberg *et al.*, Rev. Sci. Instrum. **90**, 013506 (2019).
[18] P. L. Volegov *et al.*, Rev. Sci. Instrum. **92**, 033508 (2021).
[19] R. C. Gonzalez and R. E. Woods, *Digital Image Processing* (Addison-Wesley Publishing Company, Inc., 1992).
[20] W. H. Richardson, J. Opt. Soc. Am. **62**, 55 (1972).
[21] L. B. Lucy, Astron. J. **79**, 745 (1974).
[22] J. L. Starck, E. Pantin, and F. Murtagh, Publ. Astron. Soc. Pac. **114**, 1051 (2002).
[23] R. J. Hanisch, R. L. White, and R. L. Gilliland, "Deconvolutions of Hubble space telescope images and spectra," in *Deconvolution of Images and Spectra*, 2nd ed., edited by P. A. Jansson (Academic Press, 1997).
[24] D. S. Biggs and M. Andrews, "Acceleration of iterative image restoration algorithms," Appl. Opt. **36**(8), 1766 (1997).
[25] G. J. Williams, B. R. Maddox, H. Chen, S. Kojima, and M. Millecchia, Rev. Sci. Instrum. **85**, 11E604 (2014).
[26] B. R. Maddox *et al.*, Rev. Sci. Instrum. **82**, 023111 (2011).
[27] S. P. Regan *et al.*, Fusion Sci. Technol. **73**, 89 (2018).
[28] D. Cao *et al.*, Phys. Plasmas **26**, 082709 (2019).
[29] V. Y. Glebov *et al.*, Rev. Sci. Instrum. **75**, 3559–3562 (2004).
[30] T. J. Murphy, Phys. Plasmas **21**, 072701 (2014).
[31] N. Kabadi *et al.*, Rev. Sci. Instrum. **92**, 023507 (2021).
[32] J. Ruby *et al.*, Phys. Rev. Lett. **125**, 215001 (2020).
[33] J. J. Ruby, J. A. Gaffney, J. R. Rygg, Y. Ping, and G. W. Collins, Phys. Plasmas **28**, 032703 (2021).